

Global gyrokinetic particle simulation of toroidal Alfvén eigenmodes excited by antenna and fast ions

Wenlu Zhang,^{1,2,a)} Ihor Holod,² Zhihong Lin,^{2,3} and Yong Xiao^{2,4}

¹CAS Key Laboratory of Plasma Physics, University of Science and Technology of China, Hefei, Anhui 230026, China

²Department of Physics and Astronomy, University of California, Irvine, California 92697, USA

³Fusion Simulation Center, Peking University, Beijing 100871, China

⁴Institute for Fusion Theory and Simulation, Zhejiang University, HangZhou, Zhejiang 310058, China

(Received 14 September 2011; accepted 15 January 2012; published online 22 February 2012)

Linear properties of toroidal Alfvén eigenmode (TAE) is studied in global gyrokinetic particle simulations using both fast ion and antenna excitations. A synthetic antenna provides a precise measurement of the Alfvén continuum gap width and the TAE eigenmode frequency, damping rate, and mode structures. The measured gap width exhibits a linear dependence on the aspect ratio, in agreement to a local analytic theory. The TAE frequency and mode structure excited by fast ions show a significant radial symmetry breaking relative to the ideal magnetohydrodynamic theory due to the non-perturbative contributions from the fast ions. The electromagnetic capability of the global gyrokinetic toroidal code (GTC) is verified through these global gyrokinetic simulations of Alfvén eigenmode in cylindrical and toroidal geometries. © 2012 American Institute of Physics.

[doi:10.1063/1.3685703]

I. INTRODUCTION

Energetic particles can be created in magnetically confined plasmas through fusion reactions (α -particles) and auxiliary heating such as neutral beam injection (NBI) or radio frequency (RF) heating. Generally, α -particles distributions are isotropic in velocity space, while the NBI mainly contributes to passing populations and a large portion of RF heated particles are deeply trapped particles. These energetic particles are subject to the interaction with magnetohydrodynamic (MHD) instabilities,¹ microturbulence,² stochastic magnetic field,³ and classical collisional and orbital effects.⁴ The interaction between energetic particle and background field could be two-fold: the microturbulence could affect the confinement of the energetic particles; on the other hand, they may drive a new type of instabilities, for example, Alfvén eigenmodes (AEs) and nonperturbative energetic particle modes (EPMs)⁵ *etc.* Fusion experimental^{4,6} and theoretical⁷ studies, especially recent large scale gyrokinetic particle simulations^{8,9} and NBI experiments on DIII-D,^{10,11} show that transport of high-energy α -particles by ion temperature gradient microturbulence driven by the thermal particles is negligible in burning plasmas. However, the toroidal nature of tokamak produces gaps in the continuous spectrum of Alfvén waves, which are populated by discrete, undamped shear Alfvén gap modes, for example, the toroidicity-induced Alfvén eigenmode (TAE),^{1,12–18} the reversed shear Alfvén eigenmode (RSAE),^{19,20} and the β -induced Alfvén eigenmode (BAE).^{21–23} These modes could be readily destabilized by energetic particles in burning plasmas, which induce large cross-field transport of energetic particles through wave-particle interactions and, therefore, degrades the plasma confinement.

The global gyrokinetic toroidal code (GTC)²⁴ has been successfully applied to simulate energetic particle transport

by electrostatic turbulence^{8,9} and Alfvén eigenmodes, RSAE²⁰ and BAE.²³ In this article, we will further demonstrate and verify its electromagnetic capability through a series of global gyrokinetic simulations of AEs in cylindrical and toroidal geometries. Such global gyrokinetic simulations take advantage over the MHD model that they can capture the full kinetic physics, which are essential for retaining the important background damping of various types such as collisional damping, Landau damping, continuum damping, radiative damping, *etc.* Recently, a number of gyrokinetic global codes^{13–18,25,26} have been developed to simulate the low- n TAEs. For example, Mishchenko *et al.*^{15,16} use δf particle code GYGLES, Lang *et al.*^{17,18} extended GEM code for the TAE simulations, and Lauber *et al.*^{25,26} developed a gyrokinetic eigenvalue code, LIGKA.

This paper is organized as follows. The gyrokinetic simulation model with uniform thermal plasma is described in Sec. II, the Alfvén wave simulation in cylindrical geometry is presented in Sec. III, the toroidal simulation results of TAE excitation by antenna and fast ions are presented in Sec. IV, and Sec. V summarizes this work.

II. GYROKINETIC SIMULATION MODEL

In this section, the electromagnetic gyrokinetic model used by GTC is described first. Then, the ideal MHD theory is recovered in the long wave-length limit. Next, the TAE dispersion relation is derived from the reduced equations. Finally, the TAE excitation by antenna is explained.

A. Formulation for gyrokinetic simulation

The gyrokinetic equation used to describe the plasma in toroidal systems is expressed in 5D phase space (gyrocenter position \mathbf{X} , magnetic moment μ , and parallel velocity $v_{||}$)

^{a)}Electronic mail: wlzh@ustc.edu.cn.

$$\left[\frac{\partial}{\partial t} + \dot{\mathbf{X}} \cdot \nabla + \dot{v}_{\parallel} \frac{\partial}{\partial v_{\parallel}} - C_{\alpha} \right] f_{\alpha} = 0, \quad (1)$$

$$\dot{\mathbf{X}} = v_{\parallel} \frac{\mathbf{B}}{B_0} + \mathbf{v}_E + \mathbf{v}_c + \mathbf{v}_g, \quad (2)$$

$$\dot{v}_{\parallel} = -\frac{1}{m_{\alpha} B_0} \cdot (\mu \nabla B_0 + Z_{\alpha} \nabla \phi) - \frac{Z_{\alpha}}{m_{\alpha} c} \frac{\partial A_{\parallel}}{\partial t}, \quad (3)$$

where index $\alpha = e, i, f$ stands for particle species of electron, thermal ion, and fast ion, respectively, Z_{α} is the particle charge, m_{α} is the particle mass, ϕ and A_{\parallel} are the gyroaveraged perturbation of electrostatic and vector potentials, $\mathbf{B}_0 \equiv B_0 \hat{\mathbf{b}}_0$ is the equilibrium magnetic field, $\mathbf{B} = \mathbf{B}_0 + \delta \mathbf{B}$, $\mathbf{B}^* = \mathbf{B}_0^* + \delta \mathbf{B}$, $\mathbf{B}_0^* = \mathbf{B}_0 + (B_0 v_{\parallel} / \Omega_{\alpha}) \nabla \times \hat{\mathbf{b}}_0$, $\delta \mathbf{B} = \nabla \times (A_{\parallel} \hat{\mathbf{b}}_0)$. The $\mathbf{E} \times \mathbf{B}$ drift \mathbf{v}_E , the curvature drift \mathbf{v}_c , and the grad- \mathbf{B} drift are given by

$$\mathbf{v}_E = \frac{c \hat{\mathbf{b}}_0 \times \nabla \phi}{B_0},$$

$$\mathbf{v}_c = \frac{v_{\parallel}^2}{\Omega_{\alpha}} \nabla \times \hat{\mathbf{b}}_0,$$

$$\mathbf{v}_g = \frac{\mu}{m_{\alpha} \Omega_{\alpha}} \hat{\mathbf{b}}_0 \times \nabla B_0.$$

In order to describe the properties of electrons for the meso-scale turbulence, GTC adopts the fluid-kinetic hybrid electron model, which consist of a dominant adiabatic part and a high-order kinetic response. The lowest order adiabatic part is used in this work to simulate the AEs, which is obtained by integrating the electron gyrokinetic equation in the drift-kinetic limit and gives the continuity equation of the electron density

$$\begin{aligned} \frac{\partial \delta n_e}{\partial t} + \mathbf{B}_0 \cdot \nabla \left(\frac{n_{e0} \delta u_{e\parallel}}{B_0} \right) + B_0 \mathbf{v}_E \cdot \nabla \left(\frac{n_{e0}}{B_0} \right) \\ - n_{e0} (\mathbf{v}_{e*} + \mathbf{v}_E) \cdot \frac{\nabla B_0}{B_0} = 0, \end{aligned} \quad (4)$$

where $\mathbf{v}_{e*} = \hat{\mathbf{b}}_0 \times \nabla (\delta P_{e\parallel} + \delta P_{e\perp}) / (n_{e0} m_e \Omega_e)$, $\delta P_{\parallel} = \int dv m v_{\parallel}^2 \delta f_e$, $\delta P_{e\perp} = \int d\mathbf{v} \mu B_0 \delta f_e$, $n_{e0} = \int d\mathbf{v} f_{e0}$. The electron parallel fluid velocity in the above equation can be calculated by using the parallel Ampère's law

$$n_{e0} e \delta u_{\parallel e} = \frac{c}{4\pi} \nabla_{\perp}^2 \delta A_{\parallel} + \sum_{\alpha=i,f} n_{\alpha 0} Z_{\alpha} \delta u_{\alpha\parallel}. \quad (5)$$

Here, the vector potential is obtained using the Faraday's law

$$\frac{\partial \delta A_{\parallel}}{\partial t} = \nabla_{\parallel} (\phi_{\text{eff}} - \phi) \equiv \nabla_{\parallel} \phi_{\text{ind}}. \quad (6)$$

The effective potential ϕ_{eff} is calculated by integrating the leading order terms of $\omega / (k_{\parallel} v_{\parallel})$ in the electron gyrokinetic equation assuming the uniform electron density,

$$\frac{e \phi_{\text{eff}}^{(0)}}{T_e} = \frac{\delta n_e}{n_{e0}}. \quad (7)$$

This system is closed with the gyrokinetic Poisson's equation

$$\frac{Z_i^2 n_i}{T_i} (\phi - \tilde{\phi}) = \sum_{\alpha=i,e,f} Z_{\alpha} \delta n_{\alpha}, \quad (8)$$

where $\tilde{\phi}$ is the second gyrophase-averaged potential.

A more complete formulation with non-uniform thermal plasmas can be found in Ref. 27.

B. Reduction to ideal MHD theory

We now show that the gyrokinetic simulation model retains ideal MHD modes, for example, TAE, by reducing our equations in the long wavelength limit and no parallel electric field, $\phi_{\text{eff}} = 0$. For uniform thermal plasmas, the linearized continuity equation (4) can be written

$$\frac{\partial}{\partial t} \left(\frac{\delta n_e}{n_{e0}} \right) + \mathbf{B}_0 \cdot \nabla \left(\frac{\delta u_{e\parallel}}{B_0} \right) = 0. \quad (9)$$

The Poisson equation (8) becomes

$$\frac{c^2}{4\pi e} \nabla_{\perp} \cdot \left(\frac{1}{v_A^2} \nabla_{\perp} \phi \right) = \delta n_e, \quad (10)$$

where $v_A = B_0 / \sqrt{4\pi m_i n_i}$ is the Alfvén velocity. Applying ∇_{\perp}^2 operator on Eq. (6) gives

$$\frac{1}{c} \frac{\partial}{\partial t} (\nabla_{\perp}^2 A_{\parallel}) = -\nabla_{\perp}^2 (\hat{\mathbf{b}}_0 \cdot \nabla \phi). \quad (11)$$

The inverse Ampère's law Eq. (5) reads

$$\delta u_{e\parallel} = c \frac{e}{T_e} \lambda_D^2 (\nabla_{\perp}^2 A_{\parallel}). \quad (12)$$

The ion density and ion parallel velocity have been ignored in Eqs. (10) and (12), since the ion parallel current is much smaller than the electron parallel current. Equations (9)–(12) can be combined into an eigenmode equation:

$$\frac{\partial^2}{\partial t^2} \left[\nabla_{\perp} \cdot \left(\frac{1}{v_A^2} \nabla_{\perp} \phi \right) \right] - \mathbf{B}_0 \cdot \nabla \left[\frac{1}{B_0} \nabla_{\perp}^2 (\hat{\mathbf{b}}_0 \cdot \nabla \phi) \right] = 0. \quad (13)$$

Finally, applying the Fourier transforms in time to the above equation, we arrive at

$$\omega^2 \nabla_{\perp} \cdot \left(\frac{1}{v_A^2} \nabla_{\perp} \phi \right) = -\mathbf{B}_0 \cdot \nabla \left[\frac{1}{B_0} \nabla_{\perp}^2 (\hat{\mathbf{b}}_0 \cdot \nabla \phi) \right], \quad (14)$$

which recovers the ideal MHD equations.²⁰

C. TAE dispersion relation

Now, we consider perturbations with high toroidal mode number n and use $\delta \equiv \epsilon / n \sim \mathcal{O}(k_{\parallel} / k_{\perp})$ with $\epsilon = r/a$ as an expansion parameter to develop an asymptotic solution of Eq. (14). Employing the high- n ballooning mode representation, the perturbed quantities can be expressed as

$$\phi(\Psi, \theta, \zeta) = \sum_{l=-\infty}^{\infty} \bar{\phi}(\Psi, \theta - 2\pi l, \zeta),$$

where the coordinate system (Ψ, θ, ζ) is adopted, the θ domain of $\bar{\phi}$ extends from $-\infty$ to ∞ , $2\pi\Psi$ is the poloidal flux between the magnetic axis and a constant Ψ surface. The equilibrium magnetic field $\mathbf{B}_0 = \nabla\alpha \times \nabla\Psi$, and $\alpha = \zeta - q(\Psi)\theta$ is the magnetic field line label in a toroidal system. θ and ζ are the generalized poloidal and toroidal angles with a period of 2π , and q is the safety factor and is a function of Ψ only. In this coordinate system, $\mathbf{B}_0 \cdot \nabla\theta = (\nabla\alpha \times \nabla\Psi) \cdot \nabla\theta = \mathcal{J}^{-1}$, $\mathbf{B}_0 \cdot \nabla = \mathcal{J}^{-1}\partial_\theta$, and $\mathcal{J} = q(\Psi)R^2/(B_\zeta^{(0)}R_0^2)$ is the Jacobian. It is clear that Eq. (14) is satisfied by the perturbed quantities over an infinite range in θ with no periodicity constrain. Then, we express $\bar{\phi}$ by the WKB representation,

$$\bar{\phi} = \Phi(\Psi, \theta, \delta) \exp[i\chi(\alpha, \Psi)],$$

where χ describes the rapid cross field variations and Φ is the slow variations along the field lines on the equilibrium scale, so that $\mathbf{B} \cdot \nabla\chi = 0$. For an axisymmetric toroidal system, χ is separable and can be expressed as $\chi = n(\alpha + \int \theta_k(\Psi)dq)$, where θ_k is to be determined by a higher-order radial nonlocal analysis. In the lowest order in δ , Eq. (14) then reduce to a single second-order differential equations in θ for every Ψ and θ_k . The final equation is given by

$$\mathcal{J}^{-1} \frac{\partial}{\partial\theta} \left[\frac{|\nabla\alpha|^2}{\mathcal{J}B^2} \frac{\partial}{\partial\theta} \Phi \right] + \frac{\omega^2}{v_A^2} |\nabla\alpha|^2 \Phi = 0. \quad (15)$$

For the purpose of analytical studies, we consider an axisymmetric, large aspect ratio, low- β toroidal plasma with concentric, circular magnetic surfaces, which is used as the analytic equilibrium geometry. The generalized radius, poloidal, and toroidal angles are related to the geometrical radius and angles $(\tilde{r}, \tilde{\theta}, \tilde{\zeta})$ through $\tilde{r} = r$, $\tilde{\theta} = \theta + \epsilon \sin\theta$, and $\tilde{\zeta} = \zeta$. Thus, the lab coordinate can be expressed as $x = (R_0 + \tilde{r} \cos \tilde{\theta}) \cos \tilde{\zeta}$, $y = -(R_0 + \tilde{r} \cos \tilde{\theta}) \sin \tilde{\zeta}$, $z = \tilde{r} \sin \tilde{\theta}$. Therefore, we have $|\nabla\alpha|^2 = (q'\theta)^2 + (q'/rd\theta/d\theta_r)^2 = q^2(1 + s^2\theta^2)/[r^2(1 + \epsilon \cos\theta)^2]$, where magnetic shear $s = q'r(1 + \epsilon \cos\theta)/q$. Then, the above equation can be rewritten as

$$\frac{\partial}{\partial\theta} \left[\frac{1 + s^2\theta^2}{(1 + \epsilon \cos\theta)^2} \frac{\partial}{\partial\theta} \Phi \right] + \Omega^2(1 + 4\epsilon \cos\theta) \times \frac{(1 + s^2\theta^2)}{(1 + \epsilon \cos\theta)^2} \Phi = 0.$$

If we prescribe $A = (1 + s^2\theta^2)/(1 + \epsilon \cos\theta)^2$ and $\Phi = A^{-1/2}\psi$, the high- n ballooning equation, Eq. (15), then reduces to

$$\frac{\partial^2 \psi}{\partial\theta^2} + \Omega^2(1 + 4\epsilon \cos\theta)\psi + \left(\frac{\partial^2 A/\partial\theta^2}{4A^2} \right) \psi = 0, \quad (16)$$

where $\Omega = \omega/\omega_A$, $\omega_A = v_A^{(0)}/qR_0$, $v_A^{(0)} = v_A|_{r=0}$. The last term is the origin for the TAE eigenmode. Without this term, Eq. (16) is the standard Mathieu's equation, which holds a frequency gap in the Alfvén continuum and the gap width is proportional to 2ϵ .

D. Basic theory of TAE excitation by antenna

In Sec. II C, the dispersion relation for TAE can be obtained from Eq. (16), which has been verified by TAE simulations excited by initial perturbations.¹³ Now, we are going to discuss the eigenmode excitation by antenna, which provides a way to accurately determine the eigenfrequency, damping rate, and mode structure for the damped modes in the linear and nonlinear initial value code. In GTC, the antenna is implemented through an extra synthetic potential ϕ_{ant} added to inductive potential ϕ_{ind}

$$\phi_{\text{ind}} = \phi_{\text{eff}} - \phi + \phi_{\text{ant}}$$

then Eq. (14) becomes

$$\frac{\partial^2}{\partial r^2} \left[\nabla_\perp \cdot \left(\frac{1}{v_A^2} \nabla_\perp \phi \right) \right] - \mathbf{B}_0 \cdot \nabla \left[\frac{1}{B_0} \nabla_\perp^2 (\hat{\mathbf{b}}_0 \cdot \nabla (\phi - \phi_{\text{ant}})) \right] = 0. \quad (17)$$

Suppose that a standing sinusoidal signal is loaded on the antenna at time $t = 0$,

$$\phi_{\text{ant}} = \bar{\phi}_{\text{ant}}(\Psi, \theta, \zeta) \cos(\omega_{\text{ant}}t),$$

and potential ϕ can be separated into spacial and temporal components $\phi = \phi_s(\Psi, \theta, \zeta)\phi_t(t)$. Here, the antenna drive frequency ω_{ant} is chosen close to an particular eigenfrequency ω_E of Eq. (17). Then, applying the Laplace transform to the above equation, we have

$$\Phi_t = \frac{p\phi_t(+0) + \phi_t'(+0)}{(p^2 + \omega_E^2)} + S(\Psi, \theta, \zeta) \frac{\omega_{\text{ant}}}{(p^2 + \omega_{\text{ant}}^2)(p^2 + \omega_E^2)},$$

where Φ_t is the Laplace transform of ϕ_t , $S(\Psi, \theta, \zeta)$ represents the spacial dependence. The inverse Laplace transform gives

$$\phi_t = \begin{cases} \phi_t(+0) \cos(\omega_E t) + \omega_E^{-1} \phi_t'(+0) \sin(\omega_E t) + \frac{S(\Psi, \theta, \zeta)}{2\omega_E^2} (\sin(\omega_E t) - \omega_E t \cos(\omega_E t)), & \omega_{\text{ant}} = \omega_E \\ \phi_t(+0) \cos(\omega_E t) + \omega_E^{-1} \phi_t'(+0) \sin(\omega_E t) + \frac{S(\Psi, \theta, \zeta)}{\omega_E^2 - \omega_{\text{ant}}^2} \left(\sin(\omega_{\text{ant}} t) - \frac{\omega_{\text{ant}}}{\omega_E} \sin(\omega_E t) \right), & \omega_{\text{ant}} \neq \omega_E. \end{cases} \quad (18)$$

In the first scenario, the antenna drive frequency equals to the eigenfrequency, which corresponds to a linearly growing mode with respect to time, with a frequency ω_E . However, in the second scenario, the antenna frequency is different from the eigenfrequency, and the corresponding mode is purely oscillating waves, which contains both the drive frequency ω_{ant} and the eigen-frequency ω_E .

III. ALFVÉN EIGENMODE SIMULATIONS IN CYLINDRICAL GEOMETRY

The electromagnetic capability is first demonstrated by shear Alfvén continuum spectrum in Fig. 1, where a initial perturbation is applied to the adiabatic electron density δn_e with a given mode number $m/n = 8/5$. We use a screw pinch in this simulation with a linear safety factor $q = 1.0 + r/a$ and a constant magnetic shear $s = 0.2$ in the cylindrical geometry. The stars in Fig. 1 are the Alfvén frequency measured at different radial locations in the simulation, while the solid line is the theoretical prediction $\omega = |k_{\parallel} v_A| \propto |(n - m/q)|$, where the vertical axis is normalized with the local Alfvén frequency ω_A at $r = 0.5a$.

IV. TAE EXCITATIONS BY ANTENNA

The electromagnetic capability is further demonstrated in toroidal simulation by TAE excitations using an external synthetic antenna. The eigenmode frequency, mode structure, and TAE gap size can be precisely measured in our simulation.

To recover the basic fluid properties of TAE, kinetic effects of the background thermal ions and electrons have been suppressed in the simulations in this section.

For low toroidal mode number n , the TAE mode frequency is determined by the breaking of shear Alfvén continuum spectra. Given a toroidal number n , the coupling between adjacent poloidal harmonics of Alfvén waves causes a frequency gap in the continuous spectra. The radial position r corresponding to a frequency gap is determined by the safety factor profile and toroidal/poloidal mode numbers. In our simulations, the inverse aspect ratio is 0.15 at $r = 0.5a$, safety factor has a linear profile $q = 1.0 + r/a$, and the toroidal mode number is chosen as $n = 5$. At $r = 0.5a$, $m = 7$

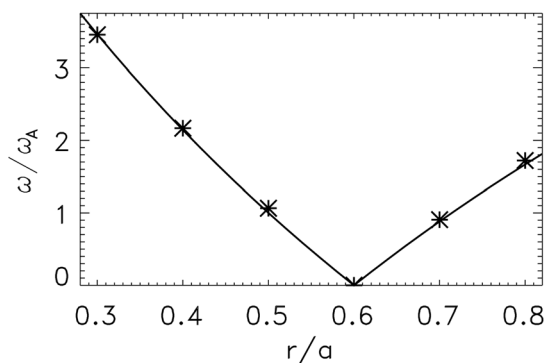


FIG. 1. Shear Alfvén frequency vs radial positions in cylindrical geometry in long wave-length limit. ω_A is the local Alfvén frequency at $r = 0.5a$.

and $m = 8$ modes have the same $|k_{\parallel}| = |n - m/q|/R$ and form the local TAE gap. The TAE eigenfrequency can be determined by the spectrum of vector potential, which is dominated by the antenna drive frequency, the upper accumulating frequency, the lower accumulating frequency, and the TAE frequency. The TAE frequency moves from right above the lower accumulating point up to the middle of the gap when magnetic shear increases. Therefore, depending on the magnetic shear, the TAE frequency and the lower accumulating point may not be well separated. In our simulation, the magnetic shear is $s = 0.2$, so the TAE frequency and the lower accumulating frequency is too close to be distinguished.

The TAE is first excited by an antenna with a frequency right in the middle of the TAE gap, $\omega_{\text{ant}} = \omega_A = v_A/(2qR)$, see Fig. 2. The upper panel is the spectrum of the antenna, the middle is the spectrum of the response vector potential A_{\parallel} , and the lower is the time history of A_{\parallel} . In the response vector potential, two dominating frequencies other than the antenna frequency are the upper accumulating frequency, and the TAE frequency (lower accumulating point), respectively. This is held naturally by Eq. (11) for an ideal MHD case, where $E_{\parallel} = 0$ and $A_{\parallel} \propto \nabla_{\parallel} \phi \propto \partial_{\theta} \phi$ for a standing wave.

Next, the antenna's frequency is set to the TAE frequency, $\omega_{\text{ant}} = \omega_{\text{TAE}}$. In this scenario, Fig. 3, the only dominate frequency in the response A_{\parallel} is the TAE eigenfrequency, and as predicted by the analytic theory, the time history of vector potential A_{\parallel} grows linearly with time because of the

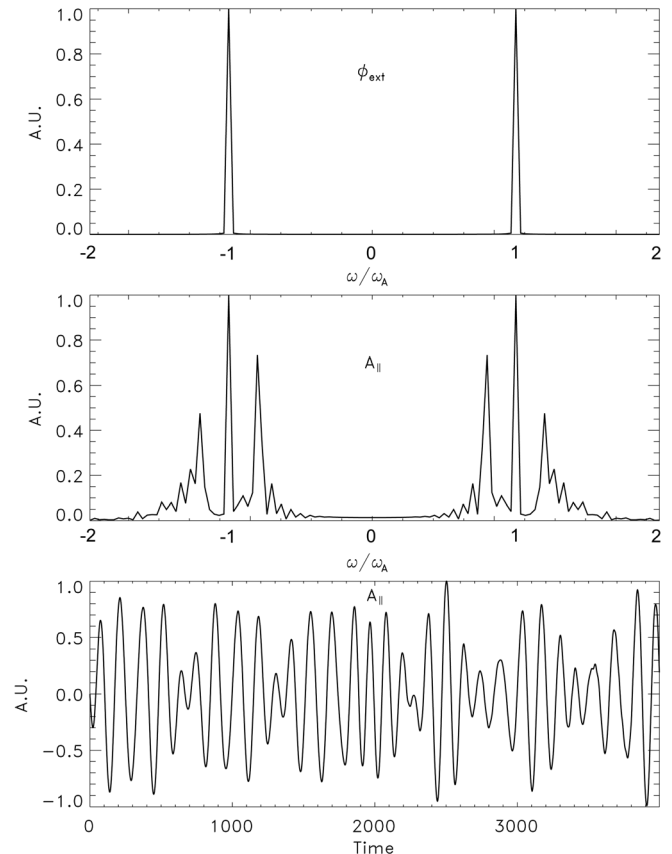


FIG. 2. Spectra of Alfvén waves excited by external drive: ϕ_{ext} (upper panel), A_{\parallel} (middle), and time history of A_{\parallel} (lower).

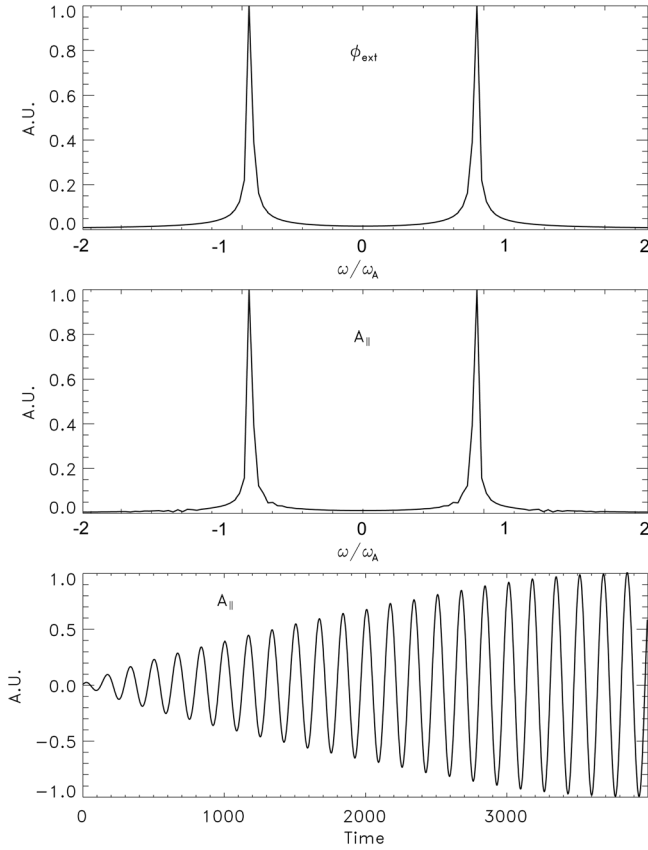


FIG. 3. Spectrum of external drive (upper panel), response $A_{||}$ (middle), and time history of $A_{||}$ (lower), where $\omega_{ext} = \omega_{TAE}$.

weak damping. As shown in Eq. (18), the width of the peaks in Fig. 3 depends on the eigen-frequencies, the driving frequency, and the number of oscillations used to calculate the mode frequency in the simulation. If damping mechanism is included in the simulation, the damping rate of the system affects the peak width as well. The mode structure is shown in Fig. 4, where the upper panel is that of the vector potential $A_{||}$ and the lower is the electrostatic potential ϕ . It is evident that the electrostatic potential shows a ballooning structure, while the vector potential shows an anti-ballooning structure.

The dominant upper accumulating frequency and TAE eigenfrequency in Fig. 2 can be used to estimate the TAE gap size. Fig. 5 shows the gap size dependence on the local aspect ratio ϵ , where the stars are simulation results for $\epsilon = 0.05, 0.1, 0.15, 0.2$, respectively. The frequency has been normalized using the Alfvén frequency $\omega_{AE} = v_A/(2qR)$. The upper and lower frequencies are fitted with solid and dotted lines, respectively, which shows a clear linear dependence to aspect ratio: $\omega/\omega_{TAE} = 1 \pm 1.35\epsilon$. This gap size is slightly bigger than the theory predictions in Sec. II, where we employed a simplified model and the third term in Eq. (16) is committed.

V. TAE EXCITATIONS BY FAST IONS

The MHD capability of gyrokinetic particle simulation is further established by the TAE excitations using fast ions.

In this section, the aspect ratio is chosen to be $a/R_0 = 0.3$ (a and R_0 are the minor and major radius of tokamak,

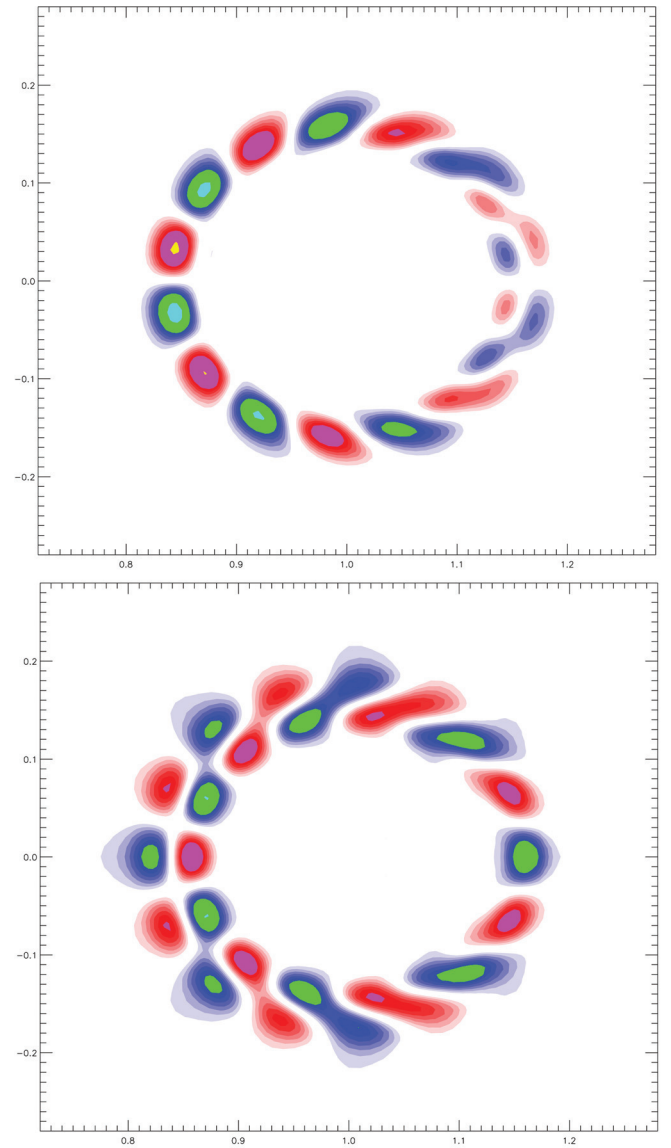


FIG. 4. (Color) Poloidal mode structure of vector potential $A_{||}$ (upper panel) and electrostatic potential ϕ (lower), where $\omega_{ext} = \omega_{TAE}$.

respectively). The fast ions are loaded with a Maxwellian distribution that holds the following on-axis parameters: $v_f = v_A, n_{f0}/n_{e0} = 0.07, a = 80\rho_f, k_0\rho_f = 0.2, \beta_e = 4\pi n_0 T_e/B_0^2 = 0.125, T_f = 16T_e$, where v_f is the thermal velocity of

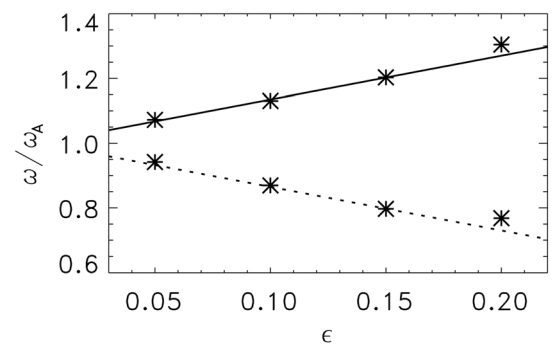


FIG. 5. TAE gap with respect to local inverse aspect ratio ϵ . The points are the pair of dominant TAE eigenfrequency and the upper accumulating frequency.

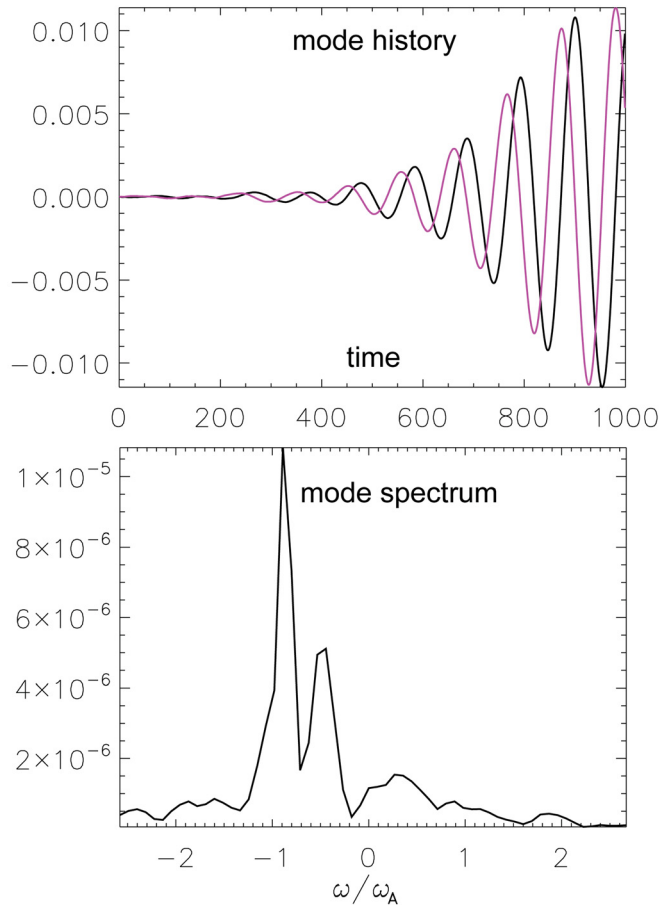


FIG. 6. (Color online) Time history of TAE mode amplitude of vector potential A_{\parallel} (upper panel) and spectrum of A_{\parallel} (lower panel), where the dominate frequency is the TAE frequency. Here, the mode number is $m=8$ and $n=5$.

the fast ions. The density gradient of fast ions peak at $r=0.5a$ and $q=1.5$ surface such that two adjacent harmonics, $m=7$ and $m=8$, dominate the $n=5$ mode. In the following part, the $m=8$ TAE harmonics of the $n=5$ mode is used as an example to investigate the linear TAE properties excited by fast ions.

As shown in Fig. 6, the fast ion excited TAE mode grows exponentially, with a growth rate of $\gamma/\omega_{\text{TAE}} \sim 6\%$, while the theory prediction¹² gives a growth rate of $\gamma/\omega_A = 8\%$. The imaginary part of the mode is $\pi/2$ leading the real part in phase, which means that this wave is a traveling wave and propagates in the fast ion diamagnetic direction. The mode frequency is slightly lower than the antenna result in Sec. III due to the nonperturbative kinetic contributions from the fast ions. The mode structure, Figs. 7 and 8, of TAE excited by fast ions shows a clear radial symmetry breaking when comparing with that excited by antenna, which is due to the nonperturbative kinetic effects of fast ions. The radial structure of the ballooning mode is determined by the radial eigenmode equation. In the local 1D theory, the ballooning mode has no radial structure (i.e., $k_r = 0$ at a poloidal angle $\theta = \theta_k$) because of the radial symmetry (Fig. 4). Any breaking of the radial symmetry, i.e., radial variations of pressure gradient and E_r etc., leads to the radial dependence of θ_k (ballooning angle). Then, the radial mode structure can be

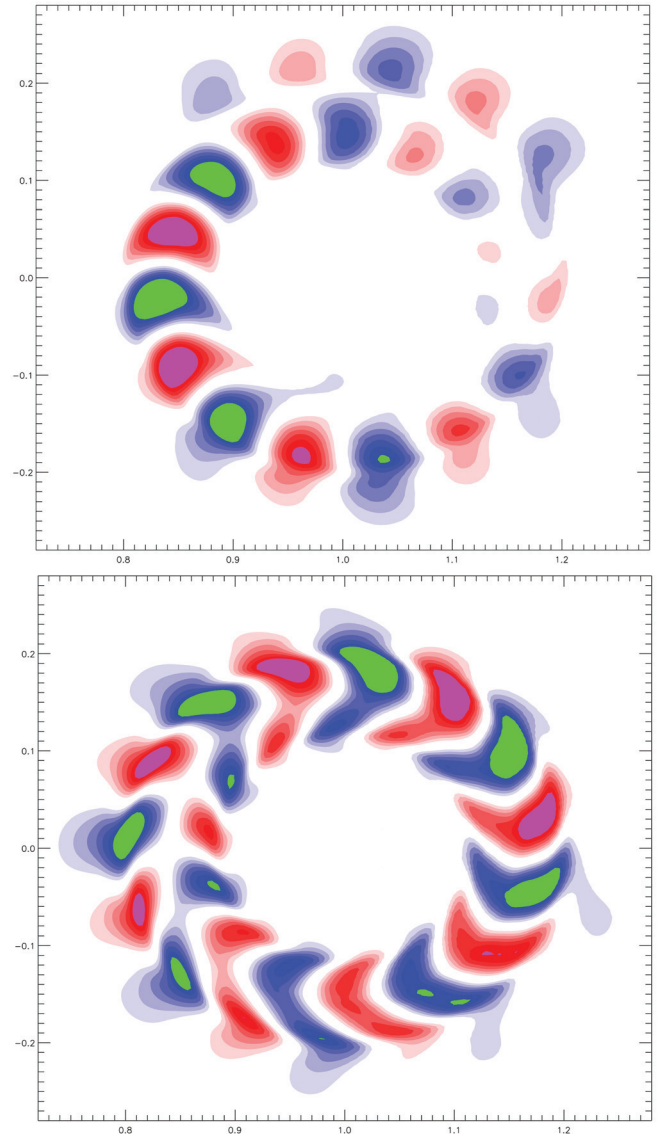


FIG. 7. (Color) Poloidal mode structure of vector potential A_{\parallel} (upper panel), and electrostatic potential ϕ (lower), where the TAE is excited by fast ions.

twisted (Fig. 7) and a 2D global eigenmode theory²⁸ is needed to solve the radial mode structure.

VI. SUMMARY

In summary, the MHD capability of gyrokinetic particle simulation has been verified through the simulations for the shear Alfvén eigenmodes in cylindrical and tokamak geometries by the GTC. A synthetic antenna is implemented in GTC to provide a way to precisely measure the eigenmode frequency, damping rate and mode structures. The Alfvén eigenmode simulation in cylindrical geometry is verified, where the measured shear Alfvén eigen-frequency dependence on the radial position agrees with the theoretical predictions. The antenna excitation provides the verifications of the TAE mode frequency, gap width, and mode structure. The measured gap size shows a linear dependence on the local aspect ratio. The TAE mode structure excited by fast ions shows a significant radial symmetry breaking relative to the

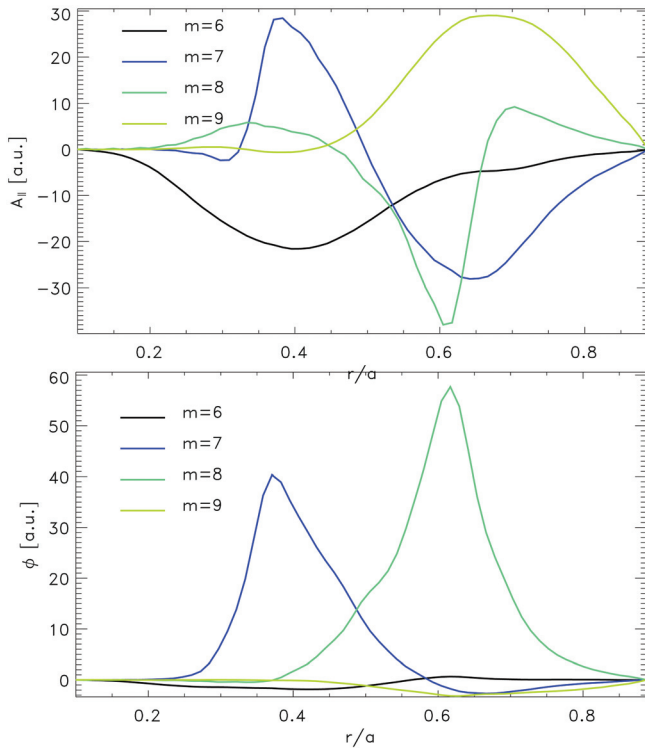


FIG. 8. (Color) Radial profiles of m -harmonics of vector potential $A_{||}$ (upper panel) and electrostatic potential ϕ (lower), for the $n=5$ mode. Here, TAE is excited by fast ions.

antenna excitation due to the nonperturbative contributions from the fast ions. Through these verifications, we demonstrated that the shear Alfvén modes can be treated accurately with the gyrokinetic PIC method.

ACKNOWLEDGMENTS

We would like to thank L. Chen and Y. Nishimura for useful discussions. This work was supported by the US Department of Energy (DOE) SciDAC GSEP center, National Natural Science Foundation of China, National Basic Research Program of China, and Nation Special Research

Program of China for ITER. Simulations used supercomputers at NERSC and ORNL.

- ¹C. Z. Cheng, L. Chen, and M. S. Chance, *Ann. Phys.* **161**, 21 (1985).
- ²W. Horton, *Rev. Mod. Phys.* **71**, 735 (1999).
- ³A. B. Rechester and M. N. Rosenbluth, *Phys. Rev. Lett.* **40**, 38 (1978).
- ⁴W. W. Heidbrink and G. J. Sadler, *Nucl. Fusion* **34**, 535 (1994).
- ⁵L. Chen, *Phys. Plasmas* **1**, 1519 (1994).
- ⁶S. J. Zweben, R. V. Budny, D. S. Darrow, S. S. Medley, R. Nazikian, B. C. Stratton, E. J. Synakowski, and G. Taylor for the TFTR Group, *Nucl. Fusion* **40**, 91 (2000).
- ⁷G. Manfredi and R. O. Dendy, *Phys. Rev. Lett.* **76**, 4360 (1996).
- ⁸W. Zhang, Z. Lin, and L. Chen, *Phys. Rev. Lett.* **101**, 095001 (2008).
- ⁹W. Zhang, V. Decyk, I. Holod, Y. Xiao, Z. Lin, and L. Chen, *Phys. Plasmas* **17**, 055902 (2010).
- ¹⁰W. W. Heidbrink, M. Murakami, J. M. Park, C. C. Petty, M. A. Van Zeeland, J. H. Yu, and G. R. McKee, *Plasma Phys. Controlled Fusion* **51**, 32 (2009).
- ¹¹W. W. Heidbrink, J. M. Park, M. Murakami, C. C. Petty, C. Holcomb, and M. A. Van Zeeland, *Phys. Rev. Lett.* **103**, 4 (2009).
- ¹²G. Y. Fu and J. W. Van Dam, *Phys. Fluids B* **1**, 1949 (1989).
- ¹³Y. Nishimura, Z. Lin, and W. X. Wang, *Phys. Plasmas* **14**, 042503 (2007).
- ¹⁴Y. Nishimura, *Phys. Plasmas* **16**, 030702 (2009).
- ¹⁵A. Mishchenko, R. Hatzky, and A. Konies, *Phys. Plasmas* **15**, 112106 (2008).
- ¹⁶A. Mishchenko, A. Konies, and R. Hatzky, *Phys. Plasmas* **16**, 082105 (2009).
- ¹⁷J. Y. Lang, Y. Chen, S. E. Parker, and G. Y. Fu, *Phys. Plasmas* **16**, 102101 (2009).
- ¹⁸Y. Chen, S. E. Parker, J. Lang, and G. Y. Fu, *Phys. Plasmas* **17**, 102101 (2010).
- ¹⁹H. L. Berk, D. N. Borba, B. N. Breizman, S. D. Pinches, and S. E. Sharapov, *Phys. Rev. Lett.* **87**, 4 (2001).
- ²⁰W. J. Deng, Z. H. Lin, I. Holod, X. Wang, Y. Xiao, and W. L. Zhang, *Phys. Plasmas* **17**, 112504 (2010).
- ²¹W. W. Heidbrink, E. J. Strait, M. S. Chu, and A. D. Turnbull, *Phys. Rev. Lett.* **71**, 855 (1993).
- ²²W. W. Heidbrink, E. Ruskov, E. M. Carolipio, J. Fang, M. A. van Zeeland, and R. A. James, *Phys. Plasmas* **6**, 1147 (1999).
- ²³H. S. Zhang, Z. Lin, I. Holod, X. Wang, Y. Xiao, and W. L. Zhang, *Phys. Plasmas* **17**, 112505 (2010).
- ²⁴Z. Lin, T. S. Hahm, W. W. Lee, W. M. Tang, and R. B. White, *Science* **281**, 1835 (1998).
- ²⁵P. Lauber, S. Gunter, and S. D. Pinches, *Phys. Plasmas* **12**, 6 (2005).
- ²⁶P. Lauber, S. Gunter, A. Konies, and S. D. Pinches, *J. Comput. Phys.* **226**, 447 (2007).
- ²⁷I. Holod, W. L. Zhang, Y. Xiao, and Z. Lin, *Phys. Plasmas* **16**, 122307 (2009).
- ²⁸F. Romanelli and F. Zonca, *Phys. Fluids B* **5**, 4081 (1993).